Many-body quantum chaos and emergence of Ginibre ensemble

Saumya Shivam,[1] Andrea De Luca,[2] David A. Huse,[1] and Amos Chan[3, 4]

[1]*Department of Physics, Princeton University, Princeton, New Jersey 08544, USA*
[2]*Laboratoire de Physique Théorique et Modélisation, CY Cergy Paris Université,*
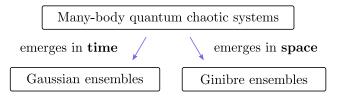*CNRS, F-95302 Cergy-Pontoise, France*
[3]*Department of Physics, Lancaster University, Lancaster LA1 4YB, United Kingdom*
[4]*Princeton Center for Theoretical Science, Princeton University, Princeton NJ 08544, USA*
(Dated: March 9, 2023)

We show that non-Hermitian Ginibre random matrix behaviors emerge in spatially-extended many-body quantum chaotic systems in the space direction, just as Hermitian random matrix behaviors emerge in chaotic systems in the time direction. Starting with translational invariant models, which can be associated with dual transfer matrices with complex-valued spectra, we show that the linear ramp of the spectral form factor necessitates that the dual spectra have non-trivial correlations, which in fact fall under the universality class of the Ginibre ensemble, demonstrated by computing the level spacing distribution and the dissipative spectral form factor. As a result of this connection, the exact spectral form factor for the Ginibre ensemble can be used to universally describe the spectral form factor for translational invariant many-body quantum chaotic systems in the scaling limit where t and L are large, while the ratio between L and $L_{\rm Th}$, the many-body Thouless length is fixed. With appropriate variations of Ginibre models, we analytically demonstrate that our claim generalizes to models without translational invariance as well. The emergence of the Ginibre ensemble is a genuine consequence of the strongly interacting and spatially extended nature of the quantum chaotic systems we consider, unlike the traditional emergence of Hermitian random matrix ensembles.

Introduction.– The discovery of the connection between quantum chaos and random matrix theory (RMT) is of great importance in theoretical physics because RMT provides an approach that eliminates dependence on the microscopic details and captures the universal characteristics of an ensemble of statistically similar chaotic systems, constrained only by symmetries [1, 2]. Historically, the spectral correlation of the Gaussian ensembles was discovered in chaotic mesoscopic systems for sufficiently small energy scales or equivalently, sufficiently late time scales [3, 4]. Recently, with the developments in random unitary circuits [5–18], particularly in time periodic or Floquet circuits, analytic calculations of random matrix behaviour in spectral correlations of spatially-extended *many-body* quantum chaotic systems have been achieved [19–27]. While Floquet circuits have given access to the study of non-trivial spectral properties in extended many-body systems — like the onset of RMT behaviour [20, 25, 27–29], spectral Lyapunov exponents [26], and novel scaling forms and limits [23, 25] — translational-invariant (TI) circuits give rise, via the so-called space-time duality, to non-Hermitian dual transfer matrix (Fig. 1 red) with complex eigenvalues, the dual spectrum. The study of many-body quantum system using space-time duality began in the study of the kicked Ising model at the self-dual point [22, 30–33] and concurrently in the transfer matrix approach in Floquet circuits [20, 25, 26]. Subsequently, numerous works have investigated the non-unitary "dynamics" in the space direction [34–38]. The objective of this paper is to provide evidence of the emergence of non-Hermitian Ginibre (GinUE) RMT-behaviour [39] in many-body quantum chaotic (MBQC) systems in the thermodynamic and scaling limit, in contrast to the emergence of standard Gaussian Hermitian RMT ensembles in late time, as illustrated below.

Many-body quantum chaotic systems

emerges in **time** ↙ ↘ emerges in **space**

Gaussian ensembles   Ginibre ensembles

Heuristics.– One of the simplest non-trivial and analytically-tractable quantities to diagnose chaos is the *spectral form factor* (SFF), defined as [2, 19–23, 25–29, 31, 41–55]

$$K(t,L) = \left\langle \left| \mathrm{Tr}_{\mathcal{H}} \left[\mathcal{W}(t,L) \right] \right|^2 \right\rangle = \left\langle \left| \mathrm{Tr}_{\tilde{\mathcal{H}}} \left[\mathcal{V}(t,L) \right] \right|^2 \right\rangle \quad (1)$$

where $\mathcal{W}(t,L) = \prod_{t'=1}^{t} W(t',L)$ is a time evolution operator acting on Hilbert space $\mathcal{H}$, and $\mathcal{V}(t,L) = \prod_{j=1}^{L} V(t,j)$ is the corresponding dual operator (Fig. 1 red) performing "evolution" in space on dual Hilbert space $\tilde{\mathcal{H}}$. t and L denote the numbers of repeated actions of W and V, and can be treated as effective time and system size respectively [56]. For Floquet systems, one has $W(t',L) = W(L)$, while $V(t,j) = V(t)$ for TI systems with transfer matrix $V(t)$. We can generally diagonalise $V(t)$ with the eigenvalues $\{z_j\} \equiv \{\rho_j e^{i\phi_j}\}$ with $\rho_j, \phi_j \in \mathbb{R}$.

$$K(t,L) = \left\langle \sum_i \rho_i^{2L} + \sum_{i \neq j} \left[e^{i(\phi_i - \phi_j)} \rho_i \rho_j \right]^L \right\rangle \quad (2)$$
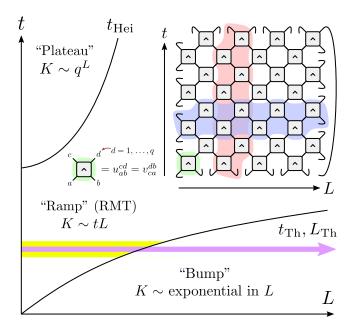
FIG. 1. Regime diagram of spectral form factor $K(t,L)$ (Eq 1) for many body quantum chaotic systems with translational invariance in space and time, with 'Bump', random matrix 'Ramp' (RMT) and 'Plateau' regimes. For fixed t and increasing L (purple), the SFF exhibits an initial linear ramp behavior (yellow) which necessarily requires non-trivial spectral statistics of the dual spectra. Inset: Diagrammatical representation of equality of the spectral form factor computed using the dual transfer matrix (Eq 1) , with unitary 2-gate (green), Floquet operator $W(L)$ (blue), dual transfer matrix $V(t)$ (red).

We are denoting as $\langle\ldots\rangle$ the ensemble average over statistically similar systems. In the absence of extra symmetries, RMT predicts $K(t,L) \sim tL$ for TI Floquet systems. This can be understood as the spectrum of $W(L)$ splits in L momentum sectors which emerges because of TI. If correlations between sectors vanish, the spectral form factor results from the sum of the usual linear-in-t behavior within each momentum sector [23]. For many-body systems, this RMT behavior emerges whenever $t > t_{\mathrm{Th}}(L)$ or equivalently $L < L_{\mathrm{Th}}(t)$, where $t_{\mathrm{Th}}(t)$, $L_{\mathrm{Th}}(L)$ are respectively the many-body SFF Thouless time and length, related by $L_{\mathrm{Th}}(t_{\mathrm{Th}}(L)) = L$. The Thouless time is a system-dependent quantity which characterises the time scale for the onset of chaos in the two-point level correlation and in general is expected to grow with system size L [23] (with the relevant exception of the dual–unitary circuits [22, 31, 36, 41, 57–59]). It is insightful to re-interpret these considerations in terms of the spectrum of $V(t)$. From Eq. (2), we see that if phase correlations could be neglected, $K(t,L) \gtrsim e^{\lambda(t)L}$, with $\lambda(t) = \max_i \ln \rho_i$ for $L \gg L_{\mathrm{Th}}(t)$. We label this regime as the "Exponential bump" region in Fig. 1. Thus, the existence of the "Ramp" regime, characteristic of RMT, for $L \lesssim L_{\mathrm{Th}}(t)$ implies that the off-diagonal term in (2) *necessarily* display non-trivial correlation, such that the

exponential behaviour of the diagonal term in (2) could be compensated. We emphasize that this heuristic argument applies to generic translational invariant MBQC systems. The characterisation of the spectral statistics of $V(t)$ will be the main objective of this letter. As we show below, such dual spectral statistics falls under the universality class of Ginibre ensemble, which can be seen as the most generic rotation invariant Gaussian ensemble, once all relevant symmetries have been taken into account (e.g. space-time translational invariance).

Models. – We consider three one-dimensional random unitary circuits as models of MBQC, namely the brick-wall model, the random phase model, and the kicked Ising model. All three models can be written as the operator $\mathcal{W}(t,L) = \prod_{t'=1}^{t} W(t',L) = \prod_{r=1}^{L} V(t,r) = \mathcal{V}(t,L)$ where $W(t',L)$ and $V(t,r)$ refer respectively to the time and space transfer matrix shown in blue and red in Fig. 1, acting on the Hilbert space with dimensions q^L and q^t respectively, with q being the on-site dimension [56]. The circuit is composed of unitary two-gates $u(t',r)$ and one can define the space-time dual of u via $u_{ab}^{cd}(t',r) = v_{ca}^{db}(t',r)$. The precise definitions of the gates $u(t',r)$ are given in the supplementary material [40], and are not crucial for our discussion as long as the models are chaotic and have no conserved quantities. We define four setups resulting from the combination of translational invariance in space and time: (a) Temporally and spatially random unitary circuits, where all u-s are drawn independently. In this case, spectral correlations are trivial in both space and time directions, with $K(t,L) \sim 1$ for all t, L [23]; (b) Temporally periodic, i.e. Floquet, and spatially random (Floquet) circuits, where $u(t',r) = u(t'',r)$ for all t', t'' and r; (c) Temporally random and spatially TI random circuits, where $u(t',r) = u(t',r')$ for all t', r and r'; and (d) Floquet and spatially TI (TIF) circuits, where $u(t',r) = u(t'',r')$ for all t',t'',r and r'.

Dual spectral statistics.– We start by focusing on TI (temporal random) models (case c), where the transfer matrix $V(t)$ has a well-defined spectrum and exhibits no additional symmetries since the model is temporarily disordered. As the spectrum is complex, in order to analyse its correlations, we resort to a) level spacing distribution and b) a natural generalization of SFF, known as the *dissipative spectral form factor* [47]. The SFF of a generic complex spectrum is exponentially growing or decaying due to the imaginary parts of the complex eigenvalues. To circumvent this problem, dissipative SFF instead treats the complex spectrum as a set of points in the plane and assess the distribution of their euclidean distances. Indeed, for a non-Hermitian operator with spectrum $\{z_n = x_n + iy_n : x_n, y_n \in \mathbb{R}\}$, the connected part is defined as

$$\mathcal{K}_c(t,s) := \left\langle \left| \sum_n e^{ix_n t + iy_n s} \right|^2 \right\rangle - \left| \left\langle \sum_n e^{ix_n t + iy_n s} \right\rangle \right|^2,$$
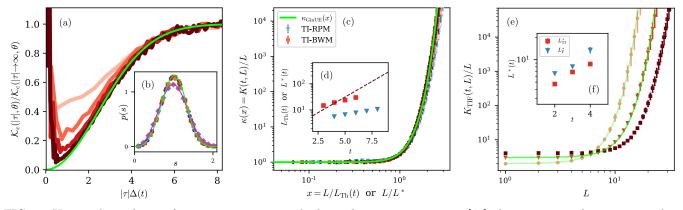$$(3)$$

FIG. 2. Universal correlations for representative many body random quantum circuits [40], showing approach to corresponding quantities computed for the Ginibre ensemble (green). (a): Dissipative spectral formm factor (3) of the dual spectra of the brick wall model, for $t = 3, 4, 5, 6$ from light to dark red. (b): Nearest neighbour spacing distribution of the dual spectra of the brick wall model (on site dimension $q = 2, t = 6$, purple), random phase model ($q = 3, t = 8$, burgundy), and zero momentum sectors of translational invariant Floquet brick wall model ($q = 2, t = 7$, red) and random phase model ($q = 3, t = 10$, gold). Kicked Ising model away from the self dual point at $J = 0.75J_c$ (grey) shows the distribution corresponding to the symmetric Ginibre ensemble (pink curve obtained from $N = 2187$) due to time reversal symmetry [40]. (c): Scaling collapse of the spectral form factor $\kappa_{TI}(x)$ for two models and $\kappa_{Gin}(x)$, for the Ginibre ensemble (8), against $x = L/L_{Th}$ or L/L^* with excellent agreement, where L_{Th} is Thouless length, and L^* is the inverse mean level spacing for Ginibre ensemble. (d): L/L_{Th} (dots) and L^* (dashed line) against time t, used for the collapse in the main panel. For Ginibre, we define an effective time via $N := q^t$. (e): Scaled spectral form factor $K_{TIF}(t, L)/L$ for translational invariant Floquet brick wall model ($q = 3, t = 2, 3, 4$, red) and the numerical fit of $K_{TIF-Gin}(t, L)/L$ (green) against L with darker colors for larger t. We fit $K_{TIF-Gin}(t, L)$ to $K_{TIF}(t, L)$ by tuning L_F^* and L_{TI}^* in Eq. (12), which are plotted against time t as blue and red respectively in (f).

where t and s are two generalized time variables. We organise them into the complex time $\tau \equiv t + is \equiv |\tau| e^{i\theta}$, and will abusively use the polar coordinate $(|\tau|, \theta)$ to parameterise the arguments of $\mathcal{K}_c$. As a yardstick for the generic behavior of $\mathcal{K}_c$, we consider the GinUE, sampled by taking N-by-N random matrices with independent complex Gaussian matrix element with variance $\sigma^2 = v/N$. In other words, the probability density for a matrix M is $\propto \exp[-N/(2v) \operatorname{Tr} MM^\dagger]$, and is thus rotational invariant. Therefore, the GinUE is expected to capture the spectral correlations of sufficiently generic, or "chaotic", complex non-Hermitian matrices, in a similar fashion to how the Gaussian and Circular unitary ensemble are the universality class for unitary and hermitian matrices respectively [47, 60]. The dissipative SFF can be computed explicitly for GinUE [47]. Keeping the leading contribution in N, $\mathcal{K}_c$ simplifies to

$$\mathcal{K}_{c,Gin}(|\tau|, \theta) = \frac{N}{v}\left(1 - e^{-\frac{v|\tau|^2}{4N}}\right). \quad (4)$$

which is rotational symmetric and shows a *(dip-)ramp-plateau* behaviour [61], analogous to the SFF for closed quantum systems: At $|\tau| \lesssim \Delta^{-1} \sim \sqrt{N}$, it increases *quadratically* $\simeq |\tau|^2/4$ in large N until it plateaus at N at a time comparable to the inverse of the mean level spacing Δ in the complex plane. Remarkably, the quadratic ramp of dissipative SFF for GinUE is drastically different from the corresponding behaviour for Gaussian unitary ensembles, which is *linear* in time. The quadratic ramp is sensitive to the variation of

density of states across the complex plane, and thus unfolding is required to uncover the true long-range dual spectral correlations [40]. In Fig. 2a, we show for TI random phase model, as a representative example, a good collapse of $\mathcal{K}_c(|\tau|, \theta)/\mathcal{K}_c(|\tau| \to \infty, \theta)$ against $|\tau|\Delta$, approaching GinUE behaviour (4) as the dual system size t increases, with a similar approach for other models [40], demonstrating universality.

To provide further evidence of emergence of GinUE, we probe the spectral correlation at the scale of mean level spacing in the complex plane using the nearest-neighbour spacing distribution in Fig. 2b, and complex spacing ratio [62] in [40], for the three different TI models. We find signatures of level repulsion consistent with the corresponding RMT universality classes (including the ones with time reversal symmetry [40]), and with the dissipative SFF results around the Δ^{-1} region.

SFF of GinUE.– With the insight that dual-spectral correlation falls under the universality class of GinUE, it is natural to ask whether this information can be used to understand the behavior of the SFF. As before, we start by focusing on TI systems, where, in the absence of extra symmetries, the correlation of the dual spectrum are captured by the standard GinUE, whose joint probability distribution function of eigenvalues $\{z_j\}$ is known exactly [63]. We model the SFF in (1), by replacing the transfer matrix $V(t)$ with V_G drawn from the GinUE of

size N, and obtain [40]

$$K_{\mathrm{Gin}}(N, L) := \left\langle \left| \mathrm{Tr}\left[V_{\mathrm{G}}^L\right]\right|^2 \right\rangle$$

$$= N^2 \delta_{L,0} + \frac{v^L \left((L+N)! - \frac{N!(N-1)!}{(N-L-1)!}\right)}{N^L (L+1)(N-1)!} \ . \tag{5}$$

In matching the predictions of (5) with many-body models, we encode t dependence in the matrix size N, whose functional form will be specified later. In the limit of large N at fixed large L, $K_{\mathrm{Gin}}(N, L) = v^L L(1 + O(L^4/N^2))$. The crossover scale $L_{\mathrm{TI}}^* = \sqrt{N}$ is related to the inverse of mean level spacing Δ in the complex plane. This suggests a scaling limit where L and N are sent to infinity with $x = L/L_{\mathrm{TI}}^*$ fixed and one has

$$\kappa_{\mathrm{Gin}}(x) \equiv \lim_{\substack{L,N\to\infty \\ x=L/L_{\mathrm{TI}}^*}} \frac{K_{\mathrm{Gin}}}{v^L L} = \frac{2\sinh\left(\frac{x^2}{2}\right)}{x^2} \ . \tag{6}$$

In fact, the above scaling form of GinUE shares similarities with the scaling forms proposed for TI (temporal random) systems in [23], given by

$$\kappa_{\mathrm{TI-MBQC}}(x) = \lim_{\substack{L,t\to\infty \\ x=L/L_{\mathrm{Th}}(t)}} \frac{K_{\mathrm{TI-MBQC}}}{L} \ , \tag{7}$$

for TI systems, where instead of L_{TI}^* in GinUE, the system-dependent many-body Thouless length $L_{\mathrm{Th}}(t)$ is used to define the scaling limit. Now, given that (i) the spectral correlation dual spectra of many body chaotic systems falls under the GinUE universality class; (ii) a linear ramp in L naturally emerges from (5) for $L \ll L_{\mathrm{TI}}^*$, coinciding with the appearance of the linear-ramp in SFF of chaotic systems; we conjecture that the scaling form of GinUE describes the scaling form of TI chaotic systems once L_{TI}^* and $L_{\mathrm{Th}}(t)$ are identified, i.e.

$$\kappa_{\mathrm{TI-MBQC}}(x) = \kappa_{\mathrm{Gin}}(x) \equiv \kappa_{\mathrm{TI-Gin}}(x) \ , \tag{8}$$

To test this claim, we simulate both sides of (8), for TI brick wall model, random phase model, and GinUE in Fig. 2c and find an excellent collapse. We note that the scaling limit in (7) differs from the infinite-q result obtained for the random phase model in [23] which disagreed with the finite-q numerical simulations. The universality of $\kappa(x)$ implies that the microscopic details are only reflected in the function $L_{\mathrm{Th}}(t)$, and not in the scaled function $\kappa(x)$, as observed in [23]. Also, the validity of Eq. (8) indicates that the effective size N of the equivalent GinUE matrix shall not be fixed from the dual Hilbert space dimension ($= q^{2t}$), but rather from the emerging Thouless length, i.e. $N = L^{*2} \sim L_{\mathrm{Th}}(t)^2 \ll q^{2t}$ (Fig. 2d).

Beyond translational invariance.– We now extend the previous considerations to Floquet systems. We first consider with spatial randomness (case b) and then we incorporate TI (case d), and demonstrate the emergence of

GinUE–like behaviour with and without TI. To incorporate time periodicity, we first observe that the transfer matrix becomes invariant under time translations, and thus its spectrum can be split in *time momentum* or frequency sectors. In the inset of Fig. 2b and [40], we respectively compute the dissipative SFF and spacing distribution for the dual spectrum in each sector, and confirm the emergence of Ginibre statistics. Time translation implies $V(t,r) = TV(t,r)T^{-1}$, where T shifts the dual system over one period. For simplicity, we assume invariance under one site translation, with $T\left|\mathbf{s} = s_1 s_2 \ldots s_t\right\rangle = \left|s_2 s_3 \ldots s_t s_1\right\rangle$, generalization to longer unit cells being straightforward. For each configuration $\mathbf{s}$, we define its associated *period* as the minimal $\tau = 1, \ldots, t$ such that $T^\tau\left|\mathbf{s}\right\rangle = \left|\mathbf{s}\right\rangle$. To formulate the statistical properties of the ensemble, we restrict the Hilbert space to the set of computational basis $\{\left|\mathbf{s}\right\rangle\}$ translational invariant with only period t. Indeed, the fraction of configurations with maximal period goes to 1 for large t (and/or obviously for large q). Using N_{o} to denote the number of distinct orbits under the translation operation, we formally have a dimension for the restricted dual Hilbert space $\dim(\tilde{\mathcal{H}}) = tN_{\mathrm{o}}$. Then, we model the transfer matrix $V(t,r)$ by a random matrix V_{G} with complex Gaussian entries and covariance

$$\left\langle [V_{\mathrm{G}}]_{\mathbf{ss'}}[V_{\mathrm{G}}]_{\mathbf{pp'}}^*\right\rangle = \frac{1}{N_{\mathrm{o}}} \sum_{\tau,\tau'} \delta_{\mathbf{s}T^\tau(\mathbf{p})} \delta_{\mathbf{s'}T^{\tau'}(\mathbf{p'})} J(\tau - \tau') \ , \tag{9}$$

where $J(\tau - \tau')$ controls the correlation between matrix elements. As pointed out in [64] via a semiclassical expansion, the emergence of SFF linear ramp using RMT $K(t) = t$ in single-particle chaotic Floquet systems can be associated to the pairing between two periodic orbits, which can happen in t possible ways (t being the discrete length of the orbit here). In extended chaotic systems, the factor of t corresponds to the possible values of $\tau = 1, \ldots, t$ for *local* pairing of orbits [20, 45]. The interaction between neighbouring local degrees of freedom forces similar pairings between local orbits, quantified here by the function $J(\tau - \tau')$. A simple calculation gives $K_{\mathrm{F-Gin}}(t, L) = \left\langle |\mathrm{Tr}[V_{\mathrm{G}}(t, L)]|^2\right\rangle = \sum_{\{\tau\}} \prod_{i=1}^{L} J(\tau_i - \tau_{i+1}) = \sum_\omega [\hat{J}(\omega)]^L$ [40], with $\hat{J}(\omega)$ the Fourier transform of $J(\tau)$. We thus see that the SFF behavior in the scaling limit depends on $\hat{J}(\omega)$. For simplicity, we suppose $J(\tau - \tau') = \delta_{\tau,\tau'} + f(t)h(\tau - \tau')$, where $f(t)$ decays to zero on the scale of the Thouless time, and the function $h(\tau - \tau')$ controls the correlation between neighbouring pairings. Within this formulation, the scaling limit depend on the details of the Fourier transform $\hat{h}(\omega)$. However, the exact calculation in the random phase model at infinite q [20, 23, 40] leads to $h(\tau - \tau') = 1 - \delta_{\tau,\tau'}$ which implies $\hat{h}(\omega) = t\delta_{\omega,0} - 1$. Numerical evidence supports the claim that in general $\hat{h}(\omega \neq 0)/\hat{h}(\omega = 0) \overset{t\to\infty}{\to} 0$. Under this assumption, one

recovers the emergent *Potts model* of SFF [40] and the universal result from [20, 23],

$$\kappa_{\mathrm{F-Gin}}(x) = \lim_{\substack{L,t \to \infty \\ x=L/L_{\mathrm{F}}^*(t)}} K_{\mathrm{F-Gin}} - t = e^x - x - 1 \,, \quad (10)$$

with $L_{\mathrm{F}}^*(t) = [f(t)\hat{h}(0)]^{-1}$. Hence, we have for case b

$$\kappa_{\mathrm{F-Gin}}(x) = \kappa_{\mathrm{F-MBQC}}(x) \,. \quad (11)$$

Translation invariant Floquet case. – For TI Floquet systems (case d), we model the transfer matrix with (9), except that TI is imposed, i.e. $V_{\mathrm{G}}(t,r) = V_{\mathrm{G}}(t,r')$ for all r, r'. In practice, Eq. (9) implies that different frequency sectors are statistically decoupled. We can thus evaluate $K_{\mathrm{TIF-Gin}}$ for this model, using Eq. (5) within each sector and replacing the variance $v/N \to \hat{J}(\omega)/N_{\mathrm{o}}$. Using the results in Eqs. (6,10), one obtains for $L \neq 0$,

$$
\begin{aligned}
K_{\mathrm{TIF-Gin}}(t,L) &= K_{\mathrm{Gin}}(N_{\mathrm{o}},L)K_{\mathrm{F-Gin}}(t,L) \\
&\sim L\,\kappa_{\mathrm{TI-Gin}}\left(\frac{L}{L_{\mathrm{TI}}^*}\right)\left[\kappa_{\mathrm{F-Gin}}\left(\frac{L}{L_{\mathrm{F}}^*}\right) + t\right] ,
\end{aligned} \quad (12)
$$

and sees that the emerging scaling form depends on the ratio between the relevant length scales, namely L_{F}^* and L_{TI}^*. For instance, if $L_{\mathrm{TI}}^* \ll L_{\mathrm{F}}^*$ at large t, the appropriate scaling limit has $x = L/L_{\mathrm{TI}}^*$ fixed, giving the scaling form

$$\kappa_{\mathrm{TIF-MBQC}}^{(\mathrm{TI})}(x) := \lim_{\substack{L,t \to \infty \\ x=L/L_{\mathrm{TI}}^*}} \frac{K_{\mathrm{TIF-Gin}}}{tL} = \kappa_{\mathrm{TI-Gin}}(x) \quad (13)$$

On the contrary, if $L_{\mathrm{F}}^* \ll L_{\mathrm{TI}}^*$ at large t, the appropriate scaling limit has $x = L/L_{\mathrm{F}}^*$ fixed leading to

$$\kappa_{\mathrm{TIF-MBQC}}^{(\mathrm{F})}(x) := \lim_{\substack{L,t \to \infty \\ x=L/L_{\mathrm{F}}^*}} \frac{K_{\mathrm{TIF-MBQC}}}{L} - t = \kappa_{\mathrm{F-Gin}}(x) \quad (14)$$

To test this, in Fig. 2e, we simulate the TI Floquet brick wall model as a representative example, and show that an excellent fit can be obtained using Eq. (12), with L_{F}^* and L_{TI}^* as fitting parameters in Fig. 2f. While we cannot determine the large-t behaviour of $L_{\mathrm{TI}}^* L_{\mathrm{F}}^*$ from the finite size data, we can extrapolate that $L_{\mathrm{TI}}^* \ll L_{\mathrm{F}}^*$ for this model, and obtain a consistent scaling collapse of (13) in [40].

Discussion. The emergence of universal Ginibre behaviour complements the known emergence of Gaussian unitary ensemble in such systems, and opens up a new avenue to characterize quantum chaos. We emphasize that the emergence of GinUE is a *many-body* quantum phenomenon: Firstly, the construction of spacetime duality requires spatial structure. Secondly, the crossover between linear ramp to exponential behaviours around L_{Th} (or t_{Th}) and the scaling collapse in the scaling limit is a manifestation of *many-body* quantum effect — the (connected) SFF of Gaussian and Circular ensembles have no exponential regime at all.

[1] M. L. Mehta, <u>Random Matrices</u> (Academic Press, 2004).

[2] F. Haake, <u>Quantum Signatures of Chaos</u> (Springer, 2010).

[3] O. Bohigas, M.-J. Giannoni, and C. Schmit, Characterization of chaotic quantum spectra and universality of level fluctuation laws, Physical Review Letters **52**, 1 (1984).

[4] A. L. Altshuler and B. I. Shklovskii, Repulsion of energy levels and conductivity of small metal samples, JETP **64**, 127 (1986).

[5] A. Nahum, J. Ruhman, S. Vijay, and J. Haah, Quantum entanglement growth under random unitary dynamics, Phys. Rev. X **7**, 031016 (2017).

[6] T. Zhou and A. Nahum, Emergent statistical mechanics of entanglement in random unitary circuits, Phys. Rev. B **99**, 174205 (2019).

[7] Y. Li, X. Chen, and M. P. A. Fisher, Quantum zeno effect and the many-body entanglement transition, Phys. Rev. B **98**, 205136 (2018).

[8] B. Skinner, J. Ruhman, and A. Nahum, Measurement-induced phase transitions in the dynamics of entanglement, Phys. Rev. X **9**, 031009 (2019).

[9] Y. Li, X. Chen, and M. P. A. Fisher, Measurement-driven entanglement transition in hybrid quantum circuits, Phys. Rev. B **100**, 134306 (2019).

[10] A. Chan, R. M. Nandkishore, M. Pretko, and G. Smith, Unitary-projective entanglement dynamics, Phys. Rev. B **99**, 224307 (2019).

[11] M. J. Gullans and D. A. Huse, Dynamical purification phase transition induced by quantum measurements, Phys. Rev. X **10**, 041020 (2020).

[12] Y. Bao, S. Choi, and E. Altman, Theory of the phase transition in random unitary circuits with measurements, Phys. Rev. B **101**, 104301 (2020).

[13] C.-M. Jian, Y.-Z. You, R. Vasseur, and A. W. W. Ludwig, Measurement-induced criticality in random quantum circuits, Phys. Rev. B **101**, 104302 (2020).

[14] A. Zabalo, M. J. Gullans, J. H. Wilson, S. Gopalakrishnan, D. A. Huse, and J. H. Pixley, Critical properties of the measurement-induced transition in random quantum circuits, Phys. Rev. B **101**, 060301 (2020).

[15] A. Nahum, S. Vijay, and J. Haah, Operator spreading in random unitary circuits, Phys. Rev. X **8**, 021014 (2018).

[16] C. W. von Keyserlingk, T. Rakovszky, F. Pollmann, and S. L. Sondhi, Operator hydrodynamics, otocs, and entanglement growth in systems without conservation laws, Phys. Rev. X **8**, 021013 (2018).

[17] T. Rakovszky, F. Pollmann, and C. W. von Keyserlingk, Diffusive hydrodynamics of out-of-time-ordered correlators with charge conservation, Phys. Rev. X **8**, 031058 (2018).

[18] V. Khemani, A. Vishwanath, and D. A. Huse, Operator spreading and the emergence of dissipation in unitary dynamics with conservation laws, ArXiv e-prints (2017), arXiv:1710.09835 [cond-mat.stat-mech].

[19] A. Chan, A. De Luca, and J. T. Chalker, Solution of a minimal model for many-body quantum chaos, Phys. Rev. X **8**, 041019 (2018).

[20] A. Chan, A. De Luca, and J. T. Chalker, Spectral statistics in spatially extended chaotic quantum many-body systems, Phys. Rev. Lett. **121**, 060601 (2018).

[21] P. Kos, M. Ljubotina, and T. Prosen, Many-body quantum chaos: The first analytic connection to random matrix theory, ArXiv e-prints (2017), arXiv:1712.02665 [nlin.CD].

[22] B. Bertini, P. Kos, and T. Prosen, Exact spectral form factor in a minimal model of many-body quantum chaos, Physical review letters **121**, 264101 (2018).

[23] A. Chan, S. Shivam, D. A. Huse, and A. De Luca, Many-body quantum chaos and space-time translational invariance, Nature communications **13**, 7484 (2022).

[24] A. Chan, A. De Luca, and J. T. Chalker, Eigenstate correlations, thermalization, and the butterfly effect, Phys. Rev. Lett. **122**, 220601 (2019).

[25] A. J. Friedman, A. Chan, A. De Luca, and J. T. Chalker, Spectral statistics and many-body quantum chaos with conserved charge, Phys. Rev. Lett. **123**, 210603 (2019).

[26] A. Chan, A. De Luca, and J. T. Chalker, Spectral lyapunov exponents in chaotic and localized many-body quantum systems, Phys. Rev. Research **3**, 023118 (2021).

[27] S. Moudgalya, A. Prem, D. A. Huse, and A. Chan, Spectral statistics in constrained many-body quantum chaotic systems, Phys. Rev. Research **3**, 023176 (2021).

[28] H. Gharibyan, M. Hanada, S. H. Shenker, and M. Tezuka, Onset of random matrix behavior in scrambling systems, Journal of High Energy Physics **2018**, 10.1007/jhep07(2018)124 (2018).

[29] P. Saad, S. H. Shenker, and D. Stanford, A semiclassical ramp in syk and in gravity (2019), arXiv:1806.06840 [hep-th].

[30] M. Akila, D. Waltner, B. Gutkin, and T. Guhr, Particle-time duality in the kicked ising spin chain, Journal of Physics A: Mathematical and Theoretical **49**, 375101 (2016).

[31] B. Bertini, P. Kos, and T. Prosen, Random matrix spectral form factor of dual-unitary quantum circuits (2021), arXiv:2012.12254 [math-ph].

[32] N. Hahn and D. Waltner, Dual approach to the spectral form factor, Acta Physica Polonica A **136**, 841 (2019).

[33] P. Braun, D. Waltner, M. Akila, B. Gutkin, and T. Guhr, Transition from quantum chaos to localization in spin chains, Phys. Rev. E **101**, 052201 (2020).

[34] A. Lerose, M. Sonner, and D. A. Abanin, Influence matrix approach to many-body floquet dynamics (2020), arXiv:2009.10105 [cond-mat.str-el].

[35] M. Ippoliti and V. Khemani, Postselection-free entanglement dynamics via spacetime duality, Phys. Rev. Lett. **126**, 060501 (2021).

[36] M. Ippoliti, T. Rakovszky, and V. Khemani, Fractal, logarithmic and volume-law entangled non-thermal steady states via spacetime duality (2021), arXiv:2103.06873 [quant-ph].

[37] T.-C. Lu and T. Grover, Entanglement transitions via space-time rotation of quantum circuits (2021), arXiv:2103.06356 [quant-ph].

[38] T.-G. Zhou, Y.-N. Zhou, P. Zhang, and H. Zhai, Space-time duality between quantum chaos and non-hermitian boundary effect (2021), arXiv:2107.01901 [cond-mat.str-el].

[39] The non-Hermitian GinUE RMT universality class is also known as non-Hermitian class A [65]. The label "U" in GinUE indicates that the distribution is invariant under unitary conjugation, although the Ginibre matrices themselves are non-unitary.

[40] See supplementary material at [url] for definitions of MBQC and Ginibre models, SFF regime diagrams, spectral properties and correlation of dual spectra, SFF analytical computations of the Ginibre ensemble and its variants, and further numerical results.

[41] A. Flack, B. Bertini, and T. Prosen, Statistics of the spectral form factor in the self-dual kicked ising model (2020), arXiv:2009.03199 [nlin.CD].

[42] J. S. Cotler, G. Gur-Ari, M. Hanada, J. Polchinski, P. Saad, S. H. Shenker, D. Stanford, A. Streicher, and M. Tezuka, Black holes and random matrices, Journal of High Energy Physics **2017**, 10.1007/jhep05(2017)118 (2017).

[43] J. Cotler, N. Hunter-Jones, J. Liu, and B. Yoshida, Chaos, complexity, and random matrices, Journal of High Energy Physics **2017**, 48 (2017).

[44] A. Altland and D. Bagrets, Quantum ergodicity in the syk model, Nuclear Physics B **930**, 45 (2018).

[45] S. J. Garratt and J. T. Chalker, Local pairing of feynman histories in many-body floquet models, Phys. Rev. X **11**, 021051 (2021).

[46] S. J. Garratt and J. T. Chalker, Many-body delocalization as symmetry breaking, Phys. Rev. Lett. **127**, 026802 (2021).

[47] J. Li, T. c. v. Prosen, and A. Chan, Spectral statistics of non-hermitian matrices and dissipative quantum chaos, Phys. Rev. Lett. **127**, 170602 (2021).

[48] D. V. Vasilyev, A. Grankin, M. A. Baranov, L. M. Sieberer, and P. Zoller, Monitoring quantum simulators via quantum nondemolition couplings to atomic clock qubits, PRX Quantum **1**, 020302 (2020).

[49] L. K. Joshi, A. Elben, A. Vikram, B. Vermersch, V. Galitski, and P. Zoller, Probing many-body quantum chaos with quantum simulators (2021), arXiv:2106.15530 [quant-ph].

[50] A. Prakash, J. H. Pixley, and M. Kulkarni, Universal spectral form factor for many-body localization, Phys. Rev. Research **3**, L012019 (2021).

[51] M. Winer, S.-K. Jian, and B. Swingle, Exponential ramp in the quadratic sachdev-ye-kitaev model, Phys. Rev. Lett. **125**, 250602 (2020).

[52] K. Wittmann W., E. R. Castro, A. Foerster, and L. F. Santos, Interacting bosons in a triple well: Preface of many-body quantum chaos, Phys. Rev. E **105**, 034204 (2022).

[53] Y. Liao, A. Vikram, and V. Galitski, Many-body level statistics of single-particle quantum chaos, Phys. Rev.

Lett. **125**, 250601 (2020).

[54] Y. Liao and V. Galitski, Emergence of many-body quantum chaos via spontaneous breaking of unitarity, Physical Review B **105**, L140202 (2022).

[55] J. Cornelius, Z. Xu, A. Saxena, A. Chenu, and A. del Campo, Spectral filtering induced by non-hermitian evolution with balanced gain and loss: Enhancing quantum chaos, Phys. Rev. Lett. **128**, 190402 (2022).

[56] The dimensions of the Hilbert space that the operator acts on in general depends on the model. For the brick-wall model in Fig. 1 (where $t = 4, L = 4$), it is q^{2t} for the time transfer matrix and q^{2L} for the space transfer matrix, q being the on-site dimension. On the other hand for the random phase model and the kicked Ising model, it is q^t for the time transfer matrix and q^L for the space transfer matrix.

[57] M. Akila, D. Waltner, B. Gutkin, and T. Guhr, Particle-time duality in the kicked ising spin chain, Journal of Physics A: Mathematical and Theoretical **49**, 375101 (2016).

[58] S. Gopalakrishnan and A. Lamacraft, Unitary circuits of finite depth and infinite width from quantum channels, Phys. Rev. B **100**, 064309 (2019).

[59] A. Lerose, M. Sonner, and D. A. Abanin, Influence matrix approach to many-body floquet dynamics, Phys. Rev. X **11**, 021040 (2021).

[60] J. Li, S. Yan, T. Prosen, and A. Chan, in preparation.

[61] At early time $|\tau| \ll \Delta^{-1}$, DSFF dips from $K(0, \theta) = N^2$ with a form described by the non-universal disconnected DSFF, $\left| \langle \sum_n e^{ix_n t + iy_n s} \rangle \right|^2$, discussed in [47], but excluded in Eq. (4) for brevity.

[62] L. Sá, P. Ribeiro, and T. c. v. Prosen, Complex spacing ratios: A signature of dissipative quantum chaos, Phys. Rev. X **10**, 021019 (2020).

[63] J. Ginibre, Statistical ensembles of complex, quaternion, and real matrices, Journal of Mathematical Physics **6**, 440 (1965), https://doi.org/10.1063/1.1704292.

[64] M. V. Berry, Semiclassical theory of spectral rigidity, Proceedings of the Royal Society of London A: Mathematical, Physical and Engineering Sciences **400**, 229 (1985).

[65] R. Hamazaki, K. Kawabata, N. Kura, and M. Ueda, Universality classes of non-hermitian random matrices, Phys. Rev. Research **2**, 023286 (2020), arXiv: 1904.13082.

[66] B. Bertini, P. Kos, and T. Prosen, Exact Spectral Form Factor in a Minimal Model of Many-Body Quantum Chaos, Phys. Rev. Lett. **121**, 264101 (2018), arXiv: 1805.00931.

[67] B. Bertini, P. Kos, and T. Prosen, Exact correlation functions for dual-unitary lattice models in 1+1 dimensions, Phys. Rev. Lett. **123**, 210601 (2019), arXiv: 1904.02140.

[68] B. Bertini, P. Kos, and T. Prosen, Operator Entanglement in Local Quantum Circuits I: Chaotic Dual-Unitary Circuits, SciPost Phys. **8**, 67 (2020).

[69] P. Braun, D. Waltner, M. Akila, B. Gutkin, and T. Guhr, Transition from quantum chaos to localization in spin chains, Phys. Rev. E **101**, 052201 (2020).

[70] G. Akemann and Z. Burda, Universal microscopic correlation functions for products of independent Ginibre matrices, J. Phys. A: Math. Theor. **45**, 465201 (2012), arXiv: 1208.0187.

[71] P. Ponte, Z. Papić, F. Huveneers, and D. A. Abanin, Many-body localization in periodically driven systems, Physical Review Letters **114**, 10.1103/physrevlett.114.140401 (2015).

[72] A. M. García-García, L. Sá, and J. J. M. Verbaarschot, Symmetry classification and universality in non-hermitian many-body quantum chaos by the sachdev-ye-kitaev model, Phys. Rev. X **12**, 021040 (2022).

[73] A. Chan, C. Dağ, and D. A. Huse, Forthcoming.

Supplementary Material

Many-body quantum chaos and emergence of Ginibre ensemble

Saumya Shivam, Andrea De Luca, David A. Huse, and Amos Chan

In this supplementary material we provide additional details about:

Appendix A: Models of MBQC

In this appendix, we explicitly write down the models studied in the main text, namely, the random phase model (RPM), the brick wall model (BWM), and the kicked ising model (KIM). Additionally, we consider an ensemble of two-site random unitary gates, which are the building blocks of random quantum circuits, and are the simplest objects that admit the space-time duality. The time evolution of a translational invariant circuit with q degrees of freedom per site can be defined by the operator $\mathcal{W}(t, L)$, which is constructed from layers of the circuit $W(t, L)$, such that the time evolution operator can be written as

$$\mathcal{W}(t, L) = \prod_{t'=1}^{t'=t} W(t', L) \, . \tag{SA.1}$$

For the case when the circuit is also periodic in time (Floquet or TIF models), we have $W(t', L) = W(L)$ for all values of t', i.e. the time evolution operator can be written as

$$\mathcal{W}(t, L) = W(L)^t . \tag{SA.2}$$

The duality transformation described in Fig. 1 results in a dual evolution operator $\mathcal{V}(t, L)$, which for both TI and TIF models are composed of DTM $V(t, r) = V(t)$ for all values of r (Fig. 1 red) according to

$$\mathcal{V}(t, L) = V(t)^L . \tag{SA.3}$$

Note that this implies that t, L denote the number of time W and V are multiplied, respectively, in order to obtain $\mathcal{W}$ and $\mathcal{V}$. The number of sites for either operator is related to t, L but depends on the model details so we provide the explicit relation for each model in the following sections. With this general notation in mind, we now describe $\mathcal{V}(t, L)$ for a two-site unitary gate and three circuit models known to show chaotic behavior, namely the RPM, the BWM, and the KIM.
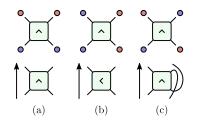
1. Two-site random unitary gate

FIG. S1. Top: Three ways of partitioning the four legs of a two-site gate into a pair of incoming (blue) and a pair of outgoing (red) tensor legs: (a) a two-site gate acting in the time direction; (b) a two-site gate acting in the space direction; (c) a two-site gate with the bottom left and top right legs as incoming legs and the rest of the legs as outgoing legs. Bottom: An alternative representation of these two-site gates, with incoming legs in the bottom and outgoing legs at the top.

A single two-site Haar-random unitary gate u_{ab}^{cd} (Fig. 1 green), having dimensions $q^2 \times q^2$, serves as a simple model to study the correlations of the dual spectrum. In our notation, the two lower indices and upper two indices of u_{ab}^{cd} label the columns and rows of the matrix u respectively. The corresponding dual gate v is defined as $v_{ca}^{db} = u_{ab}^{cd}$, where the permutation of indices correspond to space-time rotation of the two-gate.

In fact, given any two-site unitary gate (Fig. S1) which is a tensor with four legs, there are three ways to pair-wise partition the incoming and outgoing legs, namely (a) two-site gate acting in the time direction (Fig. S1a); (b) two-site gate acting in the space direction (Fig. S1b); (c) two-site gate acting in the time direction after a partial transpose (Fig. S1c). If the two-site unitary gate is drawn from the CUE (i.e. it is Haar-random), the ensemble (c) is equivalent to (b) due to the property of CUE being invariant under a unitary transformation. More explicitly, (c) can be obtained as the space-time dual of (a) after applying an additional swap gate, but since the swap gate can in fact be absorbed into the CUE, (c) is in fact equivalent to (b) for the CUE. In short, this paper studies the spectral correlation of (b) and (c) for a two-site Haar-random unitary gate, and show that they fall under the universality class of GinUE.

2. Random phase model (RPM)

The random phase model was first introduced as an analytically-tractable minimal model of many body quantum chaos without any symmetries [10], with the Floquet operator $W(L)$ consists of layers of $W(L) = W_2(L)W_1(L)$, where the layer W_1 consists of on-site Haar random unitaries u of dimension $q \times q$, and the layer W_2 consists of two-site diagonal phase gates with the phases chosen from a normal distribution with zero mean and variance ϵ. Specifically,

taking $\mathbf{b} = (b_1, \ldots, b_t)$ with $b_\mu = 1, \ldots, q$ to define the computational basis, we write

$$W_1(t) = \prod_{r=1}^{L} u(t, r) \,, \tag{SA.4a}$$

$$[W_2]_{\mathbf{b},\mathbf{b}'}(t) = \exp\left(\imath \sum_{r=1}^{L} \varphi_{b_r,b_{r+1}}(t,r) \right) \delta_{\mathbf{b},\mathbf{b}'} \,. \tag{SA.4b}$$

such that $\mathcal{W}(t, L)$ is a $q^L \times q^L$ operator, and the number of sites is L. The TI version of the circuit, where the r-dependence above is removed, was recently also shown to display chaotic behavior [23]. The layers of $W(t, L)$ can be random (TI-RPM) or repeating (TIF-RPM). Applying the duality transformation from Figure 1 on each gate leads to the dual of the single-site gate becoming a diagonal two-site gate and vice-versa for the original two-site diagonal gate. The DTM $V(t)$ for both TI-RPM and TIF-RPM, can be constructed in the following way using the two layers $V_1(t), V_2(t)$ such that $V(t) = V_2(t)V_1(t)$, where

$$[V_1]_{\mathbf{b},\mathbf{b}'}(t) = \exp\left(\imath \sum_{t'=1}^{t} \varphi_{b_{t'},b'_{t'}}(t') \right) \,, \tag{SA.5a}$$

$$[V_2]_{\mathbf{b},\mathbf{b}'}(t) = \prod_{t'=1}^{t} u_{b_{t'}}^{b_{t'+1}}(t') \delta_{\mathbf{b},\mathbf{b}'} \,, \tag{SA.5b}$$

and where periodic boundary condition has been assumed. Note that the DTM $V(t)$ inherits the same geometry as the original circuit. This also implies that $\mathcal{V}(t, L)$ is a $q^t \times q^t$ operator, and the number of corresponding sites is t. For the case of TIF-RPM, there are t momentum sectors with each block having the approximate size q^t/t. We will restrict ourselves to the zero momentum sector, which turns out to have the largest size, for the remainder of the discussion. Moreover, we only consider $q = 3$, as the circuits are not fully chaotic behavior for $q = 2$ [20].

3. Brick-wall model (BWM)

The brick-wall model is constructed with two-site $q^2 \times q^2$ Haar-random unitaries $u_{ij}^{kl}(t', r, i)$ in the brick work geometry (Fig. 1), Specifically, we have bi-layer $W(t', L) = W_2(t', L)W_1(t', L)$ consisting of two layers W_1 and W_2 defined by

$$W_i(t', L) = T_{2L}^{\delta_{i,2}} \left[\bigotimes_{r \in L} u(t', r, i) \right] T_{2L}^{-\delta_{i,2}} \,, \tag{SA.6}$$

where, again, T_n is the translational operator in the Hilbert space, $\bigotimes_1^n \mathbb{C}^q$, defined by its action on the computational basis, $T_n |\mathbf{s} \equiv s_1, s_2, \ldots, s_n\rangle = |T(\mathbf{s}) \equiv s_n, s_1, \ldots, s_{n-1}\rangle$. This means that the circuit has $2L$ sites and therefore $\mathcal{W}$ acts on a q^{2L} dimensional Hilbert space. The dual Floquet operator $V(t) = V_2(t) V_1(t)$, for TI-BWM, is then described by the two layers $V_1(t)$ and $V_2(t)$, such that in the computational basis

$$V_i(t, r) = T_{2t}^{\delta_{2,i}} \left[\bigotimes_{t'=1}^{t} v(t', r, i) \right] T_{2t}^{-\delta_{2,i}} \,, \tag{SA.7}$$

where $v(t', r, i)$ is the dual of the unitary gate $u(t', r, i)$ (with TI assumed without the r-dependence), defined by $v_{ca}^{db} = u_{ab}^{cd}$ (see Fig. 1), such that $\mathcal{V}$ acts on a q^{2t} dimensional Hilbert space.

Periodic boundary conditions have again been assumed. Note that for TIF-BWM, the unit cell in the time direction contains two sites, leading to t momentum sectors, and we will restrict ourselves to the zero momentum sector.

4. Kicked Ising model (KIM)

One of the ways in which duality of quantum circuits has been utilised is by studying a self-dual model, which arises at special points in the parameter space of the kicked Ising model, and self duality imparts analytical tractability to

proving emergence of random matrix theory through exact derivation of quantities like the spectral form factor[66–68]. The model has the same geometry as the random phase model, and the time evolution operator (acting on q^L dimensional Hilbert space) are defined using the two layers

$$W_1(t', L) = \prod_{r=1}^{L} e^{\imath h(r,t')\, \sigma_r^z} e^{\imath b\, \sigma_r^x}$$

$$W_2(t', L) = \prod_{r=1}^{L} e^{\imath J\, \sigma_r^z \sigma_{r+1}^z}$$

(SA.8)

where J and b are constants, while $h(r,t)$ is drawn from a normal distribution with variance σ^2. Note that the second layer $W_2(t', L)$ is diagonal. The DTM (acting on q^t dimensional Hilbert space) is then given by the layers

$$[V_1]_{\mathbf{b},\mathbf{b}'}(t,r) = \prod_{\mu=1}^{t} e^{\imath J b_\mu b'_\mu}$$

$$[V_2]_{\mathbf{b},\mathbf{b}'}(t,r) = \prod_{\mu=1}^{t} e^{\imath h(r,\mu)\, b_\mu} R_{b_\mu, b_{\mu+1}}\, \delta_{\mathbf{b},\mathbf{b}'}$$

(SA.9)

so that the DTM is given by $V(t,r) = V_2(t,r) V_1(t,r)$, and $R_{1,1} = R_{-1,-1} = \cos(b)$ and $R_{1,-1} = R_{1,-1} = -\imath \sin(b)$. At $|J| = |b| = \pi/4$, the dual circuit V becomes unitary which is the origin of the term "dual-unitary" for such circuits. The TI version of the model, TI-KIM, is obtained by removing the r-dependence in $h(r,t)$.

We study the dual spectra as we moves away from the self dual point, by decreasing J from $\pi/4$ to 0, while keeping $b = \pi/4$ fixed. When translational symmetry is not present, the dynamics undergo a transition when the interaction strength is reduced away from the self dual point [69]. However, for TI circuits (h_i same for each site), we don't expect the onset of many body localization, rather a transition to the non interacting integrable point at $J = 0$.

Owing to the time reversal symmetry of the original circuit, the dual circuit also has a generalized time reversal symmetry, such that there exists a unitary operator C_+ such that $C_+ V^T C_+^{-1} = V$ and $C_+ C_+^* = \mathbb{1}$. Here C_+ can be chosen to be $2^{t/2} V_2^*$ for $b = \pi/4$. Hence, instead of GinUE, the corresponding class AI† [65] (generated by choosing the complex normal variables for each matrix element such that the matrix is symmetric) is more apt for comparison. Given the lack of detailed analytic understanding of this class of non-Hermitian random matrices, we will only evaluate and compare the level spacing distribution, and look at how the dual spectrum changes when moving away from the self dual point.

Appendix B: Ginibre models of dual transfer matrices (DTM) of MBQC systems

In this appendix, we provide a summary of the variations of Ginibre ensembles as models of dual transfer matrix (DTM) of MBQC systems with translational symmetries in space and in time in Fig. S2. For systems without any symmetries, denoted as case (a) in Fig. S2, the DTM of the MBQC systems can be modelled as a sequence of matrices independently-drawn from the Ginibre ensemble, and its SFF can be computed trivially as 1 for all L, as consistent with the calculation of the MBQC circuit [23]. For Floquet systems without TI (case (b) in Fig. S2), the DTM of MBQC systems is modelled by a sequence of independently-drawn matrices satisfying Eq. (9). For TI systems with temporal randomness (case (c) in Fig. S2), the DTM of MBQC systems is modelled by the repeated action of a matrix drawn from the Ginibre ensemble. Lastly, for TI Floquet systems (case (d) in Fig. S2), the DTM of MBQC systems is modelled by the repeated action of a random matrix satisfying Eq. (9) .
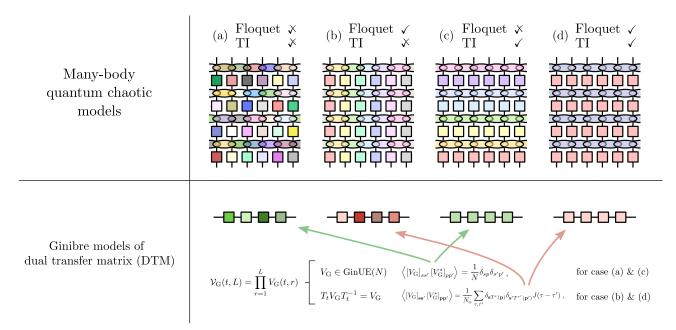
FIG. S2. Summary of variations of Ginibre ensembles as model of DTM of MBQC systems.

Appendix C: SFF regime diagrams for MBQC systems with space-time translational invariance

In this appendix, we present the regime diagrams for MBQC systems with translational invariance in space and in time in Fig. S3. Note that we focus on unitary models, such that the density of states is flat, i.e. without edges, and consequently there is not the so-called "dip" (see e.g. [28]). Note also that for temporal random MBQC systems, namely case a and c, the Heisenberg time t_{Hei} lines are absent.
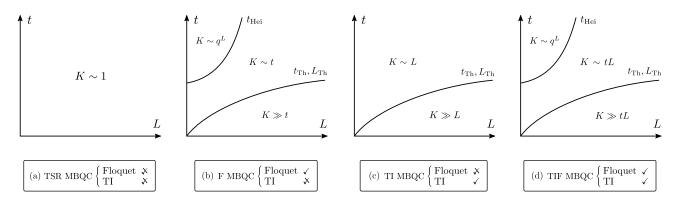

FIG. S3. SFF regime diagrams for (a) temporal and spatial random (TSR) MBQC systems; (b) temporal periodicity, i.e. Floquet, and spatial random (Floquet) MBQC systems; (c) Floquet and translational invariant (TI) MBQC systems; and (d) Floquet and translational invariant (TIF) MBQC systems.

Appendix D: Spectral properties of dual spectra

In this section, we show the distribution of eigenvalues and examples of what a typical dual spectrum looks like for the models defined in the previous section. Then, we discuss the unfolding procedure and the resulting eigenvalue distribution.
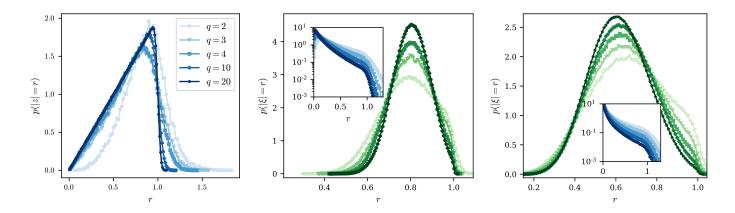
FIG. S4. Left : Radial distribution of dual eigenvalues of a two-site Haar-random unitary gate, with each site having degree of freedom q, for $q = 2, 3, 4, 10, 20$ (increasing in darkness). Middle: Distribution of the magnitude of eigenvalues of TI-BWM with $q = 2$ and $t = 3, 4, 5, 6$ with increasing darkness (inset), and the main panel shows the distribution of the magnitude of the unfolded spectrum $\xi = z^{\frac{1}{2t+1}}$. Right: Distribution of the magnitude of eigenvalues of TI-RPM with $q = 3$ and $t = 4, 5, 6, 7, 8$ with increasing darkness (inset). The main panel shows the distribution of the magnitude of the unfolded spectrum $\xi = z^{\frac{1}{t+1}}$. Using the slowly-varying regime of the unfolded spectrum, we can select of range $r_a < r < r_b$ so that for all system sizes, the distribution in that regime is approximately constant.

1. Distribution of dual eigenvalues and unfolding

In Figure S4, the distribution of the absolute value of the eigenvalues is shown for the dual of a two-site unitary gate, TI-BWM and TI-RPM as representative examples, collected from around $1000 - 5000$ random realizations. For the two-site gate, for $q > 2$, the distribution looks close to that of GinUE, which should be linear in the radial distance r until $r \approx 1$. On the other hand, for the dual circuits, the distribution is heavily concentrated close to the origin. Note that it is sufficient to look at the radial distribution because the distribution of eigenvalues is rotational symmetric upon taking disorder average, which can also be seen in a scatter plot of the spectra of single realizations of such models in Figure S5.

Since choosing a flat region from the original distribution for dual circuits can be difficult because of the power law/exponential distribution of the magnitude of eigenvalues, we take inspiration from the unfolding procedure performed in [70]. [70] considers an ensemble of products of n independent $N \times N$ matrices drawn from GinUE, and applies the conformal transformation $\xi = z^{1/n}$ [70] to the spectrum, which reveals that the ensemble eigenvalue distribution and correlations are GinUE-like. We apply the same transformation by associating n with the number of (dual) sites or the number of gates in the dual circuit. Even though the circuit geometry is different from a simple product of matrices, the transformation leads to a more slowly varying distribution of eigenvalues (Figure S4), allowing us to directly select a cutoff range of r where using rectangular strips approximately leads to flat density. It remains to be seen if there exists a transformation which can make the distribution of eigenvalues completely flat.

2. Spectra of single realizations

The spectrum of a single realizations of the dual of a two-site unitary gate, TI-RPM and a few parameters of KIM are shown in Figure S5. Note that for the dual two-site gate, the scatter plot looks uniformly spread out (with level repulsion) inside the unit disc. However for TI-BWM, they are more concentrated near the origin. Unlike both, however, TI-KIM displays a more complex structure of the spectrum. Starting with $J = J_c$ (the self dual point), the spectrum is spread out on the unit circle, owing to the unitarity. But breaking the unitarity by decreasing J/J_c leads to the eigenvalues spreading inside the unit circle in a spiral structure, which is expected to continue exhibiting level repulsion, resulting in a fractal distribution.
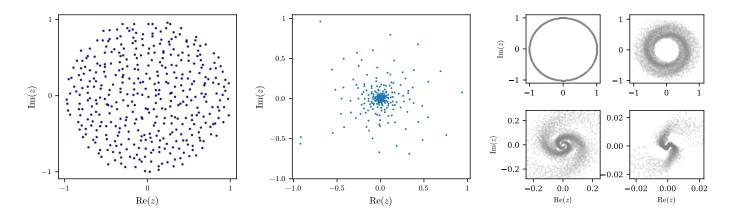
FIG. S5. Left: Spectrum of a single realization of the dual of a single two-site $q^2 \times q^2$ unitary with $q = 20$. Middle: Scatter plot of the eigenvalues of single realizations of the DTM for the RPM, with $t = 5$ and $q = 3$. Right: Scatter plot of the eigenvalues of single realizations of the DTM for the KIM, with $t = 12$ and $J/J_c = 1, 3/4, 1/2, 1/4$, clockwise from top-left, showing how starting from the self dual point, the eigenvalues collapse into a spiral, which has a fractal like structure that appears alongside level repulsion.

3. Dual spectra of non-interacting quantum circuits

In this subsection, we comment on the dual spectra of non-interacting many-body quantum circuits. The time direction quantum circuits are known to exhibit level statistics corresponding to the Poisson distribution when the quantum circuits are non-interacting or many-body localized [19, 71], and we show here that such spectral properties are also reflected in dual spectra of the dual transfer matrix. For concreteness, consider the TI-RPM (or TI-KIM) at the non-interacting point $\epsilon = 0$ ($J = 0$), where the contribution to the dual Floquet operator in Eq. SA.5 (Eq. SA.9) from the random phases becomes

$$[V_1]_{\mathbf{b},\mathbf{b}'} = 1 \tag{SD.1}$$

i.e. V_1 becomes a rank-1 matrix with where all matrix elements are one, while V_2 remains a diagonal matrix. Consequently, the dual tensor $V = V_2 V_1$ has the same elements for each column in a given row. Such a matrix has $N - 1$ zero eigenvalues, and one non zero eigenvalue ($= \text{Tr}[V_2]$).

Appendix E: Spectral correlations of dual spectra

Now we show the comparison of short and long range dual spectral statistics of various MBQC models and the GinUE, starting with nearest neighbour level spacing distribution, then the complex level spacing ratio, and finally the dissipative spectral form factor.

1. Nearest neighbour spacing distribution

The level spacing distribution of eigenvalues in the complex plane $p(s)$, can be computed by looking at the first and n^{th} nearest neighbour (in terms of the distance between the two points in the plane) for a given eigenvalue, denoted by d_1 and d_n. The unfolded level spacing is then given by $s = d_1 \sqrt{n/\pi d_n^2}$ [2], and normalized such that the mean level spacing $\int sp(s)ds = 1$. We choose n in the range $[5, 15]$, and plot the distribution of the entire spectrum over 1000 to 5000 realizations for different models in Figure S6. Whenever an additional conserved quantity is incorporated, we restrict ourselves to a given subsector or block, for example for TIF circuits, we only look at the part of the spectrum belonging to the zero momentum sector or the sector with the largest dimensions.

For the KIM, as we move from $J = \pi/4$ to $J = 0$, the level spacing distribution, after performing the appropriate unfolding (with $n = 15$ for $J < J_c$), changes from that of the Gaussian Orthogonal Ensemble (GOE) ($J = J_c$) to $\text{AI}^\dagger$ [65], for which the analytical distribution is not known, so the distribution numerically generated from symmetrized
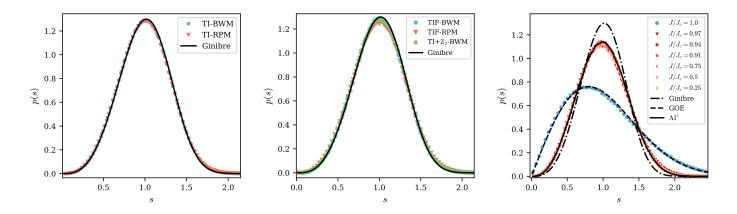
FIG. S6. Left: Unfolded and normalized level spacing distribution for dual of TI-RPM, with $q = 3$, $\epsilon = 2, t = 8$ (red), and TI-BWM with $q = 2, t = 6$ (blue) compared with the exact distribution for the complex Ginibre ensemble (solid curve) showing good agreement. Middle: Unfolded and normalized level spacing distribution in a given symmetry sector for dual circuits with different types of symmetry, compared with the exact distribution for the complex Ginibre ensemble (solid curve) showing good agreement. Right: Unfolded and normalized level spacing distribution for dual of TI-KIM, with $b = \pi/4$, $\sigma = 10\pi$ and J varying from the value at self dual point $J = \pi/4$, whose dual spectrum falls under the universality class of GOE due to the time reversal symmetry. On the other hand as soon as we move away from the self dual point, the level spacing distribution resembles that of the time reversal symmetric Ginibre universality class AI†.

GinUE matrices of size around 2000 has been plotted for comparison. The distribution for $J = 0$ is not plotted but can be shown to be the same as for TI-RPM with $\epsilon = 0$, having $N - 1$ eigenvalues zero, and a single non zero value. A summary of the universality classes for different models is given in Table S1.

Space direction	Time direction	Universality Class
Translation	None	GinUE
Translation	Translation	GinUE
Translation + TRS	TRS†	AI†

TABLE S1. Different symmetric circuits considered here, with the first two columns noting the symmetry in the space and time direction, and the third column denoting the resulting symmetry in the dual spatial direction. The third column denotes the conjectured universality class of the corresponding circuit in a given projected sector of the conserved quantity corresponding to the symmetry of the dual circuit.

2. Complex spacing ratio

Another useful quantity which also probes the angular correlations at the shortest scale is the complex level spacing ratio r [62], given for the eigenvalue z_i by

$$r_i = \frac{z_i^{\text{nn}} - z_i}{z_i^{\text{nnn}} - z_i} \tag{SE.1}$$

where z_i^{nn} and z_i^{nnn} are the nearest and next nearest distance neighbours of z respectively. The distribution of r in the complex plane has a "pac-man" shape for non-Hermitian matrices which show level repulsion [62, 72]. An advantage of this quantity is that it doesn't require unfolding of the spectra, unlike the level spacing distribution. Figure S7 shows qualitative resemblance of the distribution for TI-RPM and TI-BWM with that of the GinUE.
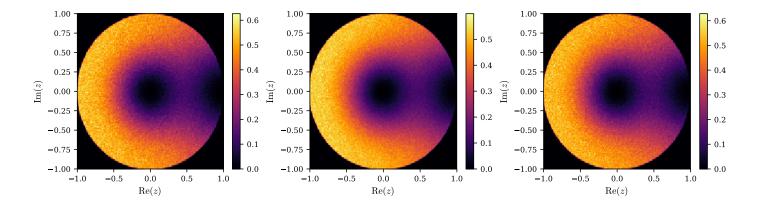
FIG. S7. Complex level spacing ratio distribution for GinUE (left), TI-RPM (middle) and TI-BWM (right), with the two dual spectra showing excellent qualitative agreement with the typical pac-man shape of level repulsion for the Ginibre ensemble. These results are consistent with the corresponding nearest neighbour level spacing distributions.

3. Dissipative spectral form factor (DSFF)

In this section, we discuss the technical details in the computation of the DSFF, including the unfolding procedure and the angular dependence, and we demonstrate the GinUE universality of the long-range spectral correlations of the dual spectra by computing DSFF for two-site Haar-random unitary gate (Fig. S9 left), TI-BWM with $q = 2$ (Fig. 2a in the main text), TI-RPM with $q = 3$ (Fig. S9 middle), and TIF-BWM with $q = 2$ (Fig. S9 right).

The quadratic ramp of (connected) DSFF is sensitive to the variation of density of states (DOS) across the complex plane — different local region of eigenvalues contribute to a ramp-plateau DSFF curves that plateau at different effective Heisenberg times, and sum to a smeared-out non-RMT-like DSFF behaviour. Therefore, the study of spectral correlation of complex spectra typically requires the complex generalization of unfolding [1], which is considerably more delicate than the real counterpart since the unfolding transformation needs to be conformal. Specifically, the (connected) DSFF, defined in Eq. 3, is computed for dual circuits after performing the unfolding procedure described in Appendix D 1. For example for the DSFF of TI-BWM in Figure 2a, the unfolded eigenvalues are $\xi = z^{\frac{1}{t+1}}$. The level spacing of original eigenvalues scale as $\Delta(t) \sim N^{-1/2} = q^{-t/2}$, and after unfolding scale as $\Delta(t) \sim 1/\sqrt{(t+1)N}$, inferred by looking at the collapse of DSFF with different dual system size t. Averages are performed around 10000 to 15000 realizations. Note that in Figure 2a and wherever not specified, the angle θ for which DSFF is computed, is chosen to be $\theta = \pi/5$ away from the axes. The DSFF for different θ for TI-BWM are shown in Figure S8, with the same unfolding procedure used. Because of rotational symmetry of eigenvalues, we see similar approaches to $\mathcal{K}_{\text{Gin}}(|\tau|)$ for different θ, except for the initial dips of the DSFF appear at different τ. However, for all of them, the dip approaches zero for larger system sizes. That scale also depends on the cutoff chosen for the eigenvalues.

Lastly, the universality of dual spectral statisticss obtained through DSFF are further argued for in Figure S9, by looking at the DSFF of the dual of two-site unitary gate with dimension $q^2 \times q^2$ A 1, arguably the simplest model with space-time duality. We see that the DSFF of the dual of this ensemble approaches the DSFF of GinUE as q increases. Note that the density of eigenvalues for $q > 2$ is roughly flat (Fig. S4), and no unfolding is required. Consqeurently, there are no dips for small $|\tau|$ in this case.

Appendix F: SFF for GinUE

1. Exact evaluation of SFF for GinUE

In this section, we evaluate the SFF for the GinUE. The definition of SFF is reproduced as follows.

$$K_{\text{Gin}}(L) = \left\langle \left| \text{Tr}[V_{\text{G}}^L] \right|^2 \right\rangle \tag{SF.1}$$
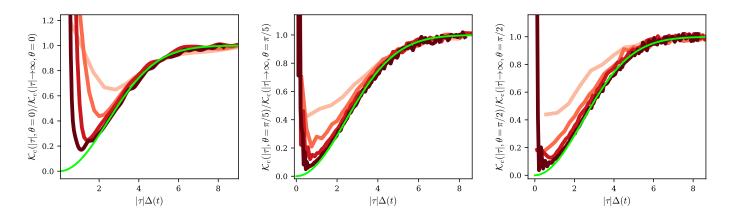
FIG. S8. θ-dependence of connected DSFF $\mathcal{K}_{\mathrm{c}}(|\tau|, \theta)$ for some choice of angles for TI-BWM with $q = 2$, $t = 6, 8, 10, 12$ (increasing in darkness), $\theta = 0$ (left), $\theta = \pi/5$ (middle) and $\theta = \pi/2$ (right). The initial dip varies with the angle. However, the location of the dip drifts toward the origin in thermodynamic limit, and the DSFF approaches the GinUE DSFF behaviour.
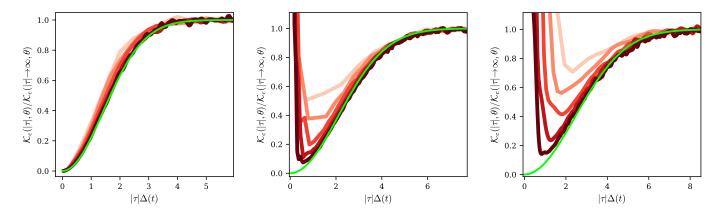

FIG. S9. Left: Connected part of the DSFF of dual of two-site $q^2 \times q^2$ Haar-random unitary gate with $\theta = \pi/4$ and $q = 2, 3, 4, 10, 20$ and the darkness increasing for larger q. The rescaled $\mathcal{K}_{\mathrm{c,Gin}}(|\tau|)$ is given as the green curve. No unfolding is performed, resulting in finite size effects for small q, although for larger q the spectrum is generally flat(Figure S4). Middle: Connected DSFF of TI-RPM with $\theta = \pi/8$, $q = 3$, and $t = 4, 5, 6, 7, 8$. Right: Connected DSFF in the zero momentum sector of TIF-BWM with $q = 2$, $\theta = \pi/16$, and $t = 6, 8, 10, 12, 14$. All three different models approach the GinUE behaviour as system sizes increase.

where V_{G} is a N-by-N matrix drawn from the GinUE with variance $\sigma^2 = v/N$, and $\langle \cdot \rangle$ is the ensemble average over the GinUE. The joint probability distribution function of eigenvalues of GinUE is known exactly, and the correlation function of eigenvalues can be expressed in terms of the kernel [63], $k(z_1, z_2) = \frac{N}{\pi v} e^{-\frac{N}{2v}(|z_1|^2 + |z_2|^2)} \sum_{\ell=0}^{N-1} \frac{1}{\ell!} \left(\frac{N z_1 z_2^*}{v} \right)^\ell$. The 1-point correlation function, i.e. the density of states, is given by $\langle \rho(z) \rangle = k(z, z)$, and the kernel is normalized such that $\int d^2 z \langle \rho(z) \rangle = \int d^2 z \, k(z, z) = N$. Note that the DOS is isotropic, and is asymptotically, as $N \to \infty$, flat on a unit disc $|z| < 1$ and vanishing outside. The 2-point correlation function is $\langle \rho(z_1) \rho(z_2) \rangle = k(z_1, z_1) \delta(z_1 - z_2) + k(z_1, z_1) k(z_2, z_2) - |k(z_1, z_2)|^2$. We will refer to the above three terms as the contact, disconnected and connected term respectively. The SFF of GinUE can now be written as

$$K_{\mathrm{Gin}}(L) = \iint d^2 z_1 d^2 z_2 \, \langle \rho(z_1) \rho(z_2) \rangle \, z_1^L z_2^{*L} \, . \tag{SF.2}$$

The contact term can be evaluated as follows

$$\int d^2z \, |z|^{2L} k(z,z) = \sum_{\ell=0}^{N-1} \frac{v^L}{N^L \ell!} (L+\ell)! = \frac{v^L (N+L)!}{N^L (L+1)(N-1)!} \,, \tag{SF.3}$$

where we have used the identity $\int_0^\infty d|z| \, |z|^{2p+1} e^{-N|z|^2/v} = \frac{1}{2} \left(\frac{v}{N}\right)^{p+1} \Gamma(p+1)$. (SF.3) is indeed N at $L=0$ as expected. The disconnected term is given by

$$\left| \int d^2z \, z^L k(z,z) \right|^2 = N^2 \delta_{L,0} \,. \tag{SF.4}$$

Lastly, the connected term can be evaluated as

$$-\int d^2z_1 \, d^2z_2 \, z_1^L z_2^{*L} \, |k(z_1,z_2)|^2 = -\int d^2z_1 \, d^2z_2 \, \frac{4N^2}{v^2} e^{-\frac{N}{2v}(|z_1|^2 + |z_2|^2)} \sum_{\ell=0}^{N-L-1} \frac{N^{L+2\ell} \, |z_1|^{2(L+\ell)+1} \, |z_2|^{2(L+\ell)+1}}{v^{L+2\ell} \, \ell! \, (L+\ell)!}$$

$$= -\sum_{\ell=0}^{N-L-1} \frac{v^L \, [(L+\ell)!]^2}{N^L \ell! (L+\ell)!} = -\frac{v^L \, N!}{N^L \, (L+1)(N-L-1)!} \,. \tag{SF.5}$$

Together, we arrive

$$K_{\text{Gin}}(L) = N^2 \delta_{L,0} + \frac{v^L \left((L+N)! - \frac{N!(N-1)!}{(N-L-1)!}\right)}{N^L (L+1)(N-1)!} \,. \tag{SF.6}$$

We reproduce the large N expansion provided in the main text below as

$$K_{\text{Gin}}(L) = v^L L \left[1 + \frac{(L-2)(L-1)L(L+1)}{24N^2} + O\left(\frac{L^8}{N^4}\right) \right] \tag{SF.7}$$

which is verified by the diagrammatical approach in large-N below.

2. Diagrammatical approach

FIG. S10. Diagrammatical representation of (a) the matrix element of matrix V_{G} drawn from the Ginibre ensemble, (b) a constraction, and (c) the (ensemble-averaged) SFF $K_{\text{Gin}}(2)$.

FIG. S11. (a) The thick line notation for a group of parallel contractions. (b) Leading diagrams in N of K_{Gin}. (c, d) Subleading diagrams of K_{Gin} of order $O\left(N^{-2}\right)$. Thick lines are colored to guide the eyes.

The diagrammatical approach of GinUE is useful as analytical tool for variations of GinUE-like models, and also as a consistency check for the exact computation of SFF (SF.6) and (SF.7) in large N. The diagrammatical approach is constructed by representing a matrix V_{G} drawn from the GinUE as in Fig. S10a, and a contraction as in in Fig. S10b. The ensemble average of the SFF of the GinUE at $L = 2$ is given as an example in Fig. S10c.

Now we verify the result in (SF.6) and (SF.7) using the diagrammatical approach in large N. Note that we fix $v = 1$ in this section. In large N, ensemble-averaged observables are dominated by diagrams with the most number of solid-line loops in the notation given in Fig. S10b (see also [19]), since each loop corresponds to a factor of N. The leading diagrams are the well-known ladder diagrams given in S11b, and it is shown in [73] that the subleading diagrams of SFF are of the form S11c and d. Firstly, We can count the degeneracy of the ladder diagran following [19]. Suppose there are L nodes in the upper trace and L nodes in the lower trace. The top left node can be chosen to contract to any one of the bottom nodes, and the rest of the nodes on the top loop have to be contracted such that a ladder is formed. Hence there are L choices, i.e. the degeneracy D_{a} of diagram S11a is

$$D_{\mathrm{b}} = L \tag{SF.8}$$

Secondly, to count diagrams in S11c, consider a realization of S11c given in Fig. S11e. We use the labels ℓ_1, ℓ_2 and ℓ_3 to denote the number of contractions in the three groups of parallel contractions. We first consider all possible diagrams with the top left node connecting with the bottom left node, colored in red in Fig. S11e. ℓ_1 can take values from 1 to $L - 2$. ℓ_2 can take $L - \ell_1 - 1$ choices. For each choices of ℓ_2, ℓ_3 is fixed since $\sum_{i=1}^{3} \ell_i = L$. Furthermore, we have to account for the fact that the red contractions can be one of any contractions in the group of ℓ_1 contractions. Finally, we unfix the contraction of the top left node and allow it to contract to any one of the L nodes in the bottom loop. This gives an additional factor of L. Therefore, we have degeneracy D_{c} given by

$$D_{\mathrm{c}} = L \sum_{\ell_1=1}^{L-2} \ell_1(L - \ell_1 - 1) = \frac{(L-2)(L-1)L^2}{6} \ . \tag{SF.9}$$

Thirdly, we can repeat the same counting argument for S11d, and obtain

$$D_{\mathrm{d}} = L \sum_{\ell_1=1}^{L-3} \ell_1 \sum_{\ell_2=1}^{L-\ell_1-2} (L - \ell_1 - \ell_2 - 1) = \frac{(L-3)(L-2)(L-1)L^2}{24} \ . \tag{SF.10}$$

Together, up to $O(N^{-2})$, we have

$$K_{\mathrm{Gin}}(L) = D_{\mathrm{b}} + \frac{1}{N^2}(D_{\mathrm{c}} + D_{\mathrm{d}}) + O\left(\frac{1}{N^4}\right) = L + \frac{(L-2)(L-1)L^2(L+1)}{24N^2} + O\left(\frac{1}{N^4}\right) \ , \tag{SF.11}$$

which verifies Eq. (SF.7).

Appendix G: SFF for Floquet GinUE model

In this appendix, we compute the SFF of a Ginibre model for the DTM of Floquet but spatially random MBQC systems, and thereby demonstrate that the emergence of GinUE-like behaviour persists beyond TI systems. The GinUE-like model is given by $\mathcal{V}(t, L) = \prod_{r=1}^{L} V_{\mathrm{G}}(t, r)$, such that $V_{\mathrm{G}}(t, r) = TV_{\mathrm{G}}(t, r)T^{-1}$, where T translates the dual

system over one period, and where we impose spatial randomness, i.e. $V_G(r) \neq V_G(r')$ for $r \neq r'$. For simplicity, we assume invariance under one site translation, with $T |\mathbf{s}\rangle = s_1 s_2 \dots s_t\rangle = |s_2 s_3 \dots s_t s_1\rangle$. Generalization to longer unit cells can be straightforwardly obtained. As described in the main text, we restrict the Hilbert space to the set of computational basis $\{|\mathbf{s}\rangle\}$ translational invariant with only period t. We note that the fraction of configurations with maximal period goes to 1 for large t (and/or obviously for large q). We demand V_G-s to have Ginibre-like correlation given by

$$\left\langle [V_G]_{\mathbf{ss}'} [V_G]^*_{\mathbf{pp}'} \right\rangle = \frac{1}{N_o} \sum_{\tau,\tau'} \delta_{\mathbf{s}T^\tau(\mathbf{p})} \delta_{\mathbf{s}'T^{\tau'}(\mathbf{p}')} J(\tau - \tau') , \tag{SG.1}$$

where N_o denotes the number of orbits, and $J(\tau)$ determines the correlation between matrix elements. Recall that s is a computational basis string, translational invariant with period t. It is convenient to represent each basis state $s = (\tilde{\mathbf{s}}, \tau)$ in terms of a representative $\tilde{\mathbf{s}}$ of the orbit and a translation parameter τ such that $s = T^\tau \tilde{s}$. In this representation, the SFF of this Floquet Ginibre model can be evaluated as the ladder diagram given in S11a and b. (Due to spatial randomness, there is only a single ladder diagram since $V_G(r)$ can only correlate with $V_G^*(r)$ for a given r.) By summing over the s degrees of freedom, the SFF can be written as

$$K(t, L) = \left\langle |\text{Tr}[V_G(t, L)]|^2 \right\rangle = \sum_{\{\tau\}} \prod_{i=1}^{L} J(\tau_i - \tau_{i+1}) = \sum_\omega [\hat{J}(\omega)]^L . \tag{SG.2}$$

where we have used the Fourier transform

$$\hat{J}(\omega) = \sum_\tau J(\tau) e^{-\frac{i 2\pi \omega \tau}{t}} , \qquad J(\tau) = \frac{1}{2\pi} \sum_\omega \hat{J}(\omega) e^{\frac{i 2\pi \omega \tau}{t}} . \tag{SG.3}$$

Now we consider a general class of correlation with $J(\tau)$ of form

$$J(\tau) = \delta_{\tau,0} + f(t) h(\tau) \tag{SG.4}$$

where $f(t)$ is some function that decays from 1 to 0 in t. Together with the first term in (SG.4), the second term ensures that there are t "domain wall" contribution, which is expected to dominate the SFF in late time [19, 20]. For simplicity, we further assume that the second term has a factorized form in t and τ. Lastly, note that in the convention of (SG.4), $h(\tau = 0) = 0$. The Fourier transform of (SG.4) is given by

$$\hat{J}(\omega) = 1 + f(t) \hat{h} \left(\frac{2\pi\omega}{t} \right) \equiv 1 + f(t) \hat{h}(\tilde{\omega}) . \tag{SG.5}$$

We will explore two cases of $J(\tau)$, namely, the fast-decaying or "short-range" and slow-decaying or "long-range" $J(\tau)$ in τ, and derive $K(L)$ and its scaling forms. In particular, when $J(\tau)$ is long-range, we recover the scaling form and an emergent Potts model, recovering the results in [20, 23], and thereby showing the emergence of Ginibre-like ensemble beyond TI MBQC systems.

1. Long-range $J(\tau)$

Suppose we take $J(\tau)$ to be long range, i.e. slow-decaying in τ. For sufficiently large t where $f(t)$ small, we substitute (SG.5) into (SG.2) and write

$$K_{\text{F-Gin}}(t, L) = \sum_\omega [1 + f(t)\hat{h}(\tilde{\omega})]^L \approx e^{f(t)\hat{h}(0)L} + \sum_{\tilde{\omega} \neq 0} e^{f(t)\hat{h}(\tilde{\omega})L} \approx e^{f(t)\hat{h}(0)L} + \frac{t-1}{2\pi} \int d\tilde{\omega} \, e^{f(t)\hat{h}(\tilde{\omega})L} . \tag{SG.6}$$

Taking $x = f(t)\hat{h}(0)L \equiv L/L^*(t)$ with $L^* \equiv [f(t)\hat{h}(0)]^{-1}$, we have

$$K_{\text{F-Gin}}(t, L) \approx e^x + \frac{t-1}{2\pi} \int d\tilde{\omega} \, e^{x\hat{h}(\tilde{\omega})/\hat{h}(0)} \approx e^x + t - 1 + \frac{(t-1)x}{2\pi} \int d\tilde{\omega} \, \frac{\hat{h}(\tilde{\omega})}{\hat{h}(0)} . \tag{SG.7}$$

To evaluate the last term, we note that

$$0 = h(\tau = 0) = \frac{t}{2\pi} \int d\tilde{\omega} \, h(\tilde{\omega}) = \hat{h}(0) + \frac{t}{2\pi} \int d\tilde{\omega} \, h(\tilde{\omega}) . \tag{SG.8}$$

Substituting this into (SG.7), we have SFF

$$K_{\mathrm{F-Gin}}(t, L) \approx e^x + t - 1 - x . \tag{SG.9}$$

and the scaling form

$$\kappa_{\mathrm{F-Gin}}(t, L) = \lim_{\substack{L,t \to \infty \\ x = L/L^*(t)}} K_{\mathrm{F-Gin}} - t = e^x - x - 1 . \tag{SG.10}$$

Consequently, we recovered the results derived in [23], i.e.

$$\kappa_{\mathrm{F-Gin}}(x) = \kappa_{\mathrm{F-MBQC}}(x) . \tag{SG.11}$$

2. Long-range $J(\tau)$ example: Emergent Potts model

As an example of long-range $J(\tau)$, we take $J(\tau)$ to be

$$J(\tau) = \delta_{\tau,0} + f(t)(1 - \delta_{\tau,0}) , \tag{SG.12}$$

with $f(t)$ vanishing for $t > t^*$, the analogue of Thouless time for this Floquet-GinUE model, we recover exactly the SFF of MBQC system evaluated at infinite-q in [20]. The fourier transform of (SG.12) gives

$$\hat{J}(\omega) = (1 - f) + t f \delta_{\omega,0} , \tag{SG.13}$$

and therefore,

$$K_{\mathrm{F-Gin}} = [1 + (t - 1)f]^L + (t - 1)(1 - f)^L . \tag{SG.14}$$

This coincides with the SFF result for Floquet MBQC systems in [20], if $f(t) = e^{-\epsilon t}$ for some parameter ϵ. Taking the scaling limit where L and t are sent large, and where $x = Ltf(t)$ fixed, we have

$$\kappa_{\mathrm{F-Gin}}(x) = \lim_{\substack{L,t \to \infty \\ x = Ltf(t)}} K_{\mathrm{F-Gin}} - t = e^x - x - 1 , \tag{SG.15}$$

which again coincides with the SFF scaling form for Floquet MBQC systems in [20]. In summary, we have

$$K_{\mathrm{F-Gin}}(t, L) = Z_{\mathrm{Potts}} = K_{\mathrm{F-MBQC}}(t, L) , \tag{SG.16}$$

where Z is the partition function of a classical t-state ferromagnetic Potts model with Boltzmann weight $\mathcal{B}(\sigma_i, \sigma_{i+1}) = \delta_{\sigma_i,\sigma_{i+1}} + f(t)(1 - \delta_{\sigma_i,\sigma_{i+1}})$ and σ_i labels the Pott state at site i. Consequently, taking the scaling limit, we have the exact identity

$$\kappa_{\mathrm{F-Gin}}(x) = \kappa_{\mathrm{F-MBQC}}(x) . \tag{SG.17}$$

3. Short-range $J(\tau)$

Suppose we take $J(\tau)$ to be short range, i.e. fast-decaying in τ. For sufficiently large t where $f(t)$ small, we substitute (SG.5) into (SG.2) and write

$$K_{\mathrm{F-Gin}}(t, L) = \sum_{\omega}[1 + f(t)\hat{h}(\tilde{\omega})]^L \approx \sum_{\omega} e^{f(t)\hat{h}(\tilde{\omega})L} \approx \frac{t}{2\pi} \int d\tilde{\omega}\, e^{f(t)\hat{h}(\tilde{\omega})L} . \tag{SG.18}$$

Casting the above equation in the scaling form, we write

$$\kappa_{\mathrm{F-Gin}}(x) = \lim_{\substack{L,t \to \infty \\ x = L/L^*(t)}} \frac{K_{\mathrm{F-Gin}}}{t} , \tag{SG.19}$$

where $L^*(t) \equiv 1/f(t)$. Importantly, this scaling form does not coincide with the analogous scaling form derived for long-range $J(\tau)$, and the results in [20, 23].

4. Short-range $J(\tau)$ example with nearest-neighbour coupling

As an example of short-range $J(\tau)$, we take

$$J(\tau) = \delta_{\tau,0} + f(t)(\delta_{\tau,1} + \delta_{\tau,-1}) \,, \tag{SG.20}$$

with Fourier transform given by

$$\hat{J}(\omega) = 1 + 2f \cos\left(\frac{2\pi\omega}{t}\right) \,, \tag{SG.21}$$

The SFF can be computed as

$$K_{\mathrm{F-Gin}}(t,L) = \sum_\omega [1 + 2f\cos(\tilde\omega)]^L \approx \frac{t}{2\pi}\int d\tilde\omega \, e^{2f(t)\cos(\tilde\omega)L} = tI(2f(t)L) \,, \tag{SG.22}$$

where I is the Bessel function.

Appendix H: SFF for TI Floquet GinUE model

In this appendix, we compute the SFF of a Ginibre model for the DTM of TIF MBQC systems. The TIF Ginibre model is given by $\mathcal{V}(t,L) = \prod_{r=1}^L V_{\mathrm{G}}(t,r)$, with $V_{\mathrm{G}}(t,r)$ satisfying $V_{\mathrm{G}}(t,r) = TV_{\mathrm{G}}(t,r)T^{-1}$, $V_{\mathrm{G}}(t,r) = V_{\mathrm{G}}(t,r')$ for all r,r' and (9). Recall that T translates the dual system over one period. We will use the same representation for the basis state $\mathbf{s} = (\tilde{\mathbf{s}},\tau)$, as in Appendix G, where $\tilde{\mathbf{s}}$ is a representative of the orbit of $\mathbf{s}$, and τ is a parameter such that $\mathbf{s} = T^\tau\tilde{\mathbf{s}}$. In this representation, the matrix elements of V is given by,

$$V_{\mathbf{ss}'}^{\tau\tau'} \equiv \langle \mathbf{s}',\tau'| V |\mathbf{s},\tau\rangle = V_{\mathbf{ss}'}^{\tau-\tau'} \tag{SH.1}$$

where the last equality is due to $V_{\mathrm{G}}(t,r) = TV_{\mathrm{G}}(t,r)T^{-1}$, and we have left the subscript G implicit. Using the Fourier transformation $|\mathbf{s},\tau\rangle = (2\pi)^{-1/2}\sum_\omega e^{i2\pi\tau\omega/t}|\mathbf{s},\omega\rangle$ and $|\mathbf{s},\omega\rangle = (2\pi)^{-1/2}\sum_t e^{-i2\pi\tau\omega/t}|\mathbf{s},t\rangle$, we write

$$\langle \mathbf{s}',\omega'| V |\mathbf{s},\omega\rangle = \delta_{\omega,\omega'}\sum_\tau e^{-i2\pi\tau\omega/t}V_{\mathbf{ss}'}^\tau \tag{SH.2}$$

We can then rewrite the covariance,

$$\left\langle V_{\mathbf{s}_1\mathbf{s}_2}^\tau V_{\mathbf{s}_3\mathbf{s}_4}^{*\tau'}\right\rangle = \frac{J(\tau-\tau')}{N_{\mathrm{o}}}\delta_{\mathbf{s}_1,\mathbf{s}_2}\delta_{\mathbf{s}_3,\mathbf{s}_4} \tag{SH.3}$$

in the frequency space as

$$\left\langle V_{\mathbf{s}_1\mathbf{s}_2}^\omega V_{\mathbf{s}_3\mathbf{s}_4}^{*\omega'}\right\rangle = \delta_{\omega\omega'}\frac{\hat{J}(\omega)}{N_{\mathrm{o}}}\delta_{\mathbf{s}_1,\mathbf{s}_2}\delta_{\mathbf{s}_3,\mathbf{s}_4} \tag{SH.4}$$

where $V_{\mathbf{ss}'}^\omega \equiv \langle \mathbf{s}',\omega| V |\mathbf{s},\omega\rangle$. Eq. (SH.4) means that different frequency sectors are statistically decoupled. Noting that matrix elements of V in (SH.4) behave like matrix elements of a Ginibre matrix, with variance $v/N \to \hat{J}(\omega)/N_{\mathrm{o}}$. We can thus evaluate $K_{\mathrm{TIF-Gin}}$ for this model, using Eq. (5) within each frequency sector and obtain for $L \neq 0$,

$$\begin{aligned}
K_{\mathrm{TIF-Gin}}(t,L) &= \frac{\left((L+N_{\mathrm{o}})! - \frac{N_{\mathrm{o}}!(N_{\mathrm{o}}-1)!}{(N_{\mathrm{o}}-L-1)!}\right)}{N_{\mathrm{o}}^L(L+1)(N_{\mathrm{o}}-1)!}\sum_\omega \left[\hat{J}(\omega)\right]^L \\
&= K_{\mathrm{Gin}}(N_{\mathrm{o}},L)K_{\mathrm{F-Gin}}(t,L) \\
&\sim L\,\kappa_{\mathrm{TI-Gin}}\left(\frac{L}{L_{\mathrm{TI}}^*}\right)\left[\kappa_{\mathrm{F-Gin}}\left(\frac{L}{L_{\mathrm{F}}^*}\right) + t\right] \,,
\end{aligned} \tag{SH.5}$$

where in the last line, we have used the results in Eqs. (6,10).

Appendix I: SFF: Numerical results

In this section, we provide further scaling collapses of the TIF-BWM as a representative model of TIF MBQC systems. From the numerical fitting in 2f, we have $L_F^* < L_{TI}^*$ for TIF-BWM. This motivates us to plot the scaling collapse according to Eq. (13) in Fig. S12, and we see that agreement is obtained with the scaling function provided in Eq. (13). Lastly, note that $L_{Th}(t)$ is computed by looking at the intersection points of $K_{TI}(t, L)/L$ vs L with a horizontal line close to 1 (see also the Appendices in [23]), and averaged over around 10000 to 15000 realizations.
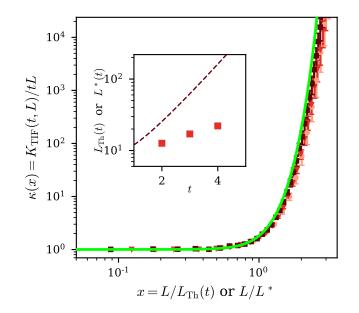

FIG. S12. Scaling collapse of $K_{TIF}(t, L)/tL$ against x for TIF-BWM with $q = 3$, $t = 2, 3, 4$ (reds), also shown in Fig. 2e. The scaling form K_{TIF}/tL agrees with $\kappa_{GinUE}(x)$ in Eq. 13. The inset shows the corresponding $L_{Th}(t)$ and $L^*(t)$ against t.